How to calibrate an object-adapted optical trap for force sensing and interferometric shape tracking of asymmetric structures

Matthias Koch[1] and Alexander Rohrbach[1,2,*]

[1]*Laboratory for Bio- and Nano-Photonics, Department of Microsystems Engineering-IMTEK, University of Freiburg, Germany*

[2]*Centre for Biological Signalling Studies (bioss), University of Freiburg, Germany*

[*]*rohrbach@imtek.de*

Abstract: Optical traps have shown to be a flexible and powerful tool for 3D manipulations on the microscale. However, when it comes to sensitive measurements of particle displacements and forces thorough calibration procedures are required, which can be already demanding for trapped spheres. For asymmetric structures, with more complicated shapes, such as helical bacteria, novel calibration schemes need to be established. The paper describes different methods of how to extract various calibration parameters of a tiny helical bacterium, which is trapped and tracked in shape by scanning line optical tweezers. Tiny phase differences of the light scattered at each slope of the bacterium are measured by back focal plane interferometry, providing precise and high bandwidth information about fast deformations of the bacterium. A simplified theoretical model to estimate the optical forces on a chain like structure is presented. The methods presented here should be of interest to people that investigate optical trapping and tracking of asymmetric particles.

OCIS codes: (350.4855) Optical tweezers or optical manipulation; (170.5810) Scanning microscopy; (170.1420) Biology; (260.3160) Interference; (290.0290) Scattering.

References and links

1. F. Wang, W. J. Toe, W. M. Lee, D. McGloin, Q. Gao, H. H. Tan, C. Jagadish, and P. J. Reece, "Resolving Stable Axial Trapping Points of Nanowires in an Optical Tweezers Using Photoluminescence Mapping," Nano Lett. **13**(3), 1185–1191 (2013).
2. M. Grießhammer and A. Rohrbach, "5D-Tracking of a nanorod in a focused laser beam - a theoretical concept," Opt. Express **22**(5), 6114–6132 (2014).
3. L. P. Faucheux, G. Stolovitzky, and A. Libchaber, "Periodic Forcing of a Brownian Particle," Phys. Rev. E Stat. Phys. Plasmas Fluids Relat. Interdiscip. Topics **51**(6), 5239–5250 (1995).
4. G. Carmon, P. Kumar, and M. Feingold, "Optical tweezers assisted imaging of the Z-ring in Escherichia coli: measuring its radial width," New J. Phys. **16**(1), 013043 (2014).
5. M. Brunner, J. Dobnikar, H. H. von Grünberg, and C. Bechinger, "Direct measurement of three-body interactions amongst charged colloids," Phys. Rev. Lett. **92**(7), 078301 (2004).
6. J. C. Crocker, J. A. Matteo, A. D. Dinsmore, and A. G. Yodh, "Entropic attraction and repulsion in binary colloids probed with a line optical tweezer," Phys. Rev. Lett. **82**(21), 4352–4355 (1999).
7. M. Speidel, L. Friedrich, and A. Rohrbach, "Interferometric 3D tracking of several particles in a scanning laser focus," Opt. Express **17**(2), 1003–1015 (2009).
8. B. Tränkle, M. Speidel, and A. Rohrbach, "Interaction dynamics of two colloids in a single optical potential," Phys. Rev. E Stat. Nonlin. Soft Matter Phys. **86**(2), 021401 (2012).
9. V. Demergis and E. L. Florin, "High precision and continuous optical transport using a standing wave optical line trap," Opt. Express **19**(21), 20833–20848 (2011).
10. D. B. Ruffner and D. G. Grier, "Optical Conveyors: A Class of Active Tractor Beams," Phys. Rev. Lett. **109**(16), 163903 (2012).
11. R. Nambiar, A. Gajraj, and J. C. Meiners, "All-optical constant-force laser tweezers," Biophys. J. **87**(3), 1972–1980 (2004).
12. L. P. Faucheux, L. S. Bourdieu, P. D. Kaplan, and A. J. Libchaber, "Optical thermal ratchet," Phys. Rev. Lett. **74**(9), 1504–1507 (1995).
13. S. Trachtenberg and R. Gilad, "A bacterial linear motor: cellular and molecular organization of the contractile cytoskeleton of the helical bacterium Spiroplasma melliferum BC3," Mol. Microbiol. **41**(4), 827–848 (2001).

#220691 - $15.00 USD Received 12 Aug 2014; revised 24 Sep 2014; accepted 25 Sep 2014; published 8 Oct 2014

14. M. Koch and A. Rohrbach, "Object-adapted optical trapping and shape-tracking of energy-switching helical bacteria," Nat. Photonics **6**(10), 680–686 (2012).
15. M. Mahamdeh, C. P. Campos, and E. Schäffer, "Under-filling trapping objectives optimizes the use of the available laser power in optical tweezers," Opt. Express **19**(12), 11759–11768 (2011).
16. H. Kress, E. H. K. Stelzer, G. Griffiths, and A. Rohrbach, "Control of relative radiation pressure in optical traps: Application to phagocytic membrane binding studies," Phys. Rev. E Stat. Nonlin. Soft Matter Phys. **71**(6), 061927 (2005).
17. L. Friedrich and A. Rohrbach, "Tuning the detection sensitivity: a model for axial backfocal plane interferometric tracking," Opt. Lett. **37**(11), 2109–2111 (2012).
18. T. A. Nieminen, V. L. Y. Loke, A. B. Stilgoe, G. Knöner, A. M. Brańczyk, N. R. Heckenberg, and H. Rubinsztein-Dunlop, "Optical tweezers computational toolbox," J. Opt. A, Pure Appl. Opt. **9**(8), S196–S203 (2007).
19. A. Rohrbach, C. Tischer, D. Neumayer, E. L. Florin, and E. H. K. Stelzer, "Trapping and tracking a local probe with a photonic force microscope," Rev. Sci. Instrum. **75**(6), 2197–2210 (2004).
20. K. Svoboda and S. M. Block, "Biological applications of optical forces," Annu. Rev. Biophys. Biomol. Struct. **23**(1), 247–285 (1994).
21. A. Pralle, M. Prummer, E. L. Florin, E. H. K. Stelzer, and J. K. H. Hörber, "Three-dimensional high-resolution particle tracking for optical tweezers by forward scattered light," Microsc. Res. Tech. **44**(5), 378–386 (1999).
22. B. E. A. Saleh and M. C. Teich, *Fundamentals of Photonics* (John Wiley, 1991).
23. D. B. Phillips, S. H. Simpson, J. A. Grieve, R. Bowman, G. M. Gibson, M. J. Padgett, J. G. Rarity, S. Hanna, M. J. Miles, and D. M. Carberry, "Force sensing with a shaped dielectric micro-tool," Europhys. Lett. **99**(5), 58004 (2012).

1. Introduction

Taking a picture of a person from the top does not provide much information, since humans, like most other mammalians, are lengthy in shape. Therefore, the optical imaging axis is usually chosen to be perpendicular to the long axis of a person. On a much smaller scale, conventional optical traps usually orient lengthy objects (or several round objects) along the optical imaging axis, since the intensity gradient is weakest in this direction [1,2]. This makes detailed imaging of more complicated, lengthy structures difficult or even impossible.

Therefore, alternative optical traps have to be designed to manipulate and investigate complex, dynamic and force producing structures, which are relevant to bio- and nano-technology. Such light distributions, which are characterized by strong radial intensity gradients, can be generated either by time-multiplexing a highly focused laser beam (optical point trap) [3] or by a static line-focus resulting from phase holograms. Also called line optical tweezers, these elongated traps have shown to be useful for orienting bacteria in the image plane during fluorescence based investigations of the Z-ring of single E.Coli cells [4], investigating static and dynamic [5–8] particle interactions as well as transport processes [9, 10]. Therefore, the intensity along the trap center line is modulated such that harmonic optical potentials [7], linear potential ramps [11] or periodic potentials [12] are created, enabling various particle transport modes or force measurements.

Line traps can be calibrated by standard methods for spherical and cylindrical particles. However, the equivalent force calibration for complex shaped structures such as helical bacteria [13] is trickier. Only recently, we have shown that 200 nm thin living helical bacteria (spiroplasma melliferum), which quickly undergo fast shape deformations, can be trapped and oriented by smoothly distributing the optical energy along the bacterium with a time-multiplexed point trap [14]. The deformations could be measured by interference of unscattered trapping light and light scattered specifically at each slope of the bacterium. By this interferometric shape tracking, a 3D movie with very high contrast and resolution could be recorded at 800 Hz. The measured slope deformation enabled us to estimate the deformation energy the bacterium had to bring up against the optical forces, against viscous friction of the embedding fluid and against its own internal strains.

In this paper we show both experimentally and theoretically, how linear restoring forces arise in all three directions even for complex shaped structures, enabling precise force measurements, which can be spatially resolved along the axis of the bacterium. We further show how to calibrate such an objected adapted optical trap and the inherent interferometric tracking system. The current study bases on the supplementary information of our recent publication [14].

#220691 - $15.00 USD Received 12 Aug 2014; revised 24 Sep 2014; accepted 25 Sep 2014; published 8 Oct 2014

2. Optical setup

The task of capturing a lively, deforming bacterium purely by optical forces and to distribute the optical energy as smoothly as possible along the bacterium is not trivial. In time average, the helical bacterium needs to experience linear restoring forces in all three directions, i.e., an elongated 3D harmonic optical potential must be created. The requirements for an optical trapping and tracking setup that exerts well-controlled optical forces and precisely measures shape deformations by using a time-multiplexed laser focus is explained in the following:

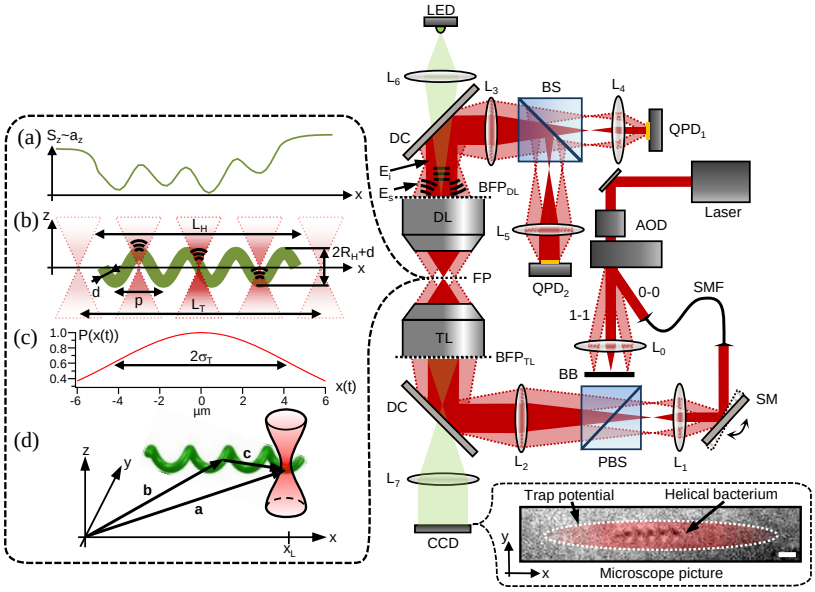

Fig. 1. Setup scheme for time multiplexed optical trapping and tracking. A 1064 nm laser passes an acousto optic deflector (AOD). The different diffraction orders are used for two independently steerable optical traps. Interference of light scattered at a trapped object with the unscattered light is analyzed by two quadrant photo diodes (QPDs). For further details see main text. A Köhler-illumination from the top is used to image the focal plane on a CCD with the aid of lens L_7. Right inset: Brightfield image of a trapped bacterium with the optical line trap indicated by a red ellipse (reproduced from [14]). Scale bar: 1 µm. Left inset: (a) Axial signal from QPD_2. (b) Different trap positions forming the time shared optical potential. A projection of the helical cell is shown in green together with the cell tube diameter d, the helical pitch p and the overall cell diameter $D + d$. (c) Distribution of incident intensity along the line trap. (d) Illustration of the coordinate system and vector definitions (reproduced from [14]).

A two axis acousto optic deflector (two AODs – DTSXY-400-1064, AA Opto Electronics) is used to mainly modulate the intensity I_0 of a 2 W 1064 nm cw laser (Smart Laser Systems, Germany) by controlling the transmitted power $P(x(t))\cdot I_0$. Instead of an AOD, a simple acousto-optic modulator (AOM) can be also used. The non-diffracted 0th orders beam (0-0) is used for the intensity modulation and is coupled into a single mode fiber (SMF), to be deflected by a two axis galvanometric scan mirror (SM - General Scanning Inc., Watertown, MA) enabling a maximum scan frequency of f_{SM} = 1000 Hz. Two laterally displaced beams (in bright red) and one non-displaced beam (in dark red) are illustrated in Fig. 1. In principle, the first orders (1-1) diffracted beam from the AOD can be used, too, if fast scan frequencies are required and slight intensity aberrations from the AOD are acceptable. Since the 0th orders and 1st orders diffracted beams are orthogonally polarized, they can be easily re-combined by a polarizing beam splitter cube (PBS). However, in our study the (1-1) orders beam diffracted by the AOD was only used in section 6, but not for the regular experiments. As the beams diffracted by only one AOD (0-1 and 1-0), it was thus blocked by a beam block (BB).

#220691 - $15.00 USD Received 12 Aug 2014; revised 24 Sep 2014; accepted 25 Sep 2014; published 8 Oct 2014

The non-diffracted beam (0-0) deflected by the SM is then imaged through a 4 f-system (L1-L2) onto the back focal plane (BFP_{TL}) of the trapping lens (TL – Olympus UPLAPO60X/IR) with numerical aperture NA = 1.2. In this way, the diffraction limited laser focus can be displaced by $x_L = \pm 6$ µm at 500 Hz in the focal plane (FP) of the TL resulting in a time-multiplexed optical point trap. Trapping parameters can be further adjusted by over- or underfilling of BFP_{TL} [15,16] by the lens system L_0/L_2 and L_1/L_2, respectively. In general, the laser focus is displaced at several 100 Hz along a line (x direction) using the SM in order to adapt the trapping potential to the elongated helical cell body (as indicated by the inset of Fig. 1, thus creating an intensity modulated line trap [3,7,8,14] (also see section 3).

The incident laser light as well as the coherently scattered light is collected by another high NA objective lens (Zeiss 440067 63x Achroplan NA 0.95), also referred to as detection lens (DL). The BFP_{DL} of the DL is imaged by two different lens systems L_3/L_4 and L_3/L_5 on two InGaAs quadrant photo diodes (G6849, Hamamatsu Photonics), where the interference pattern is analyzed for shape tracking of the trapped cell (see section 4). In principle, one QPD would be sufficient but the usage of two different effective NAs for lateral and axial position detection leads to a better signal quality [17].

An additional bright field LED illumination (green) from top is used to image the focal plane on a CCD camera (Visitron Systems GmbH, CoolSNAP cf). The trapping light and the illumination beam are separated by a dichroic mirror (DC).

3. Theory: Forces and potentials of a helical structure in a line optical trap

In this section we address the question from a theoretical point of view, whether a soft structure with a complicated shape, such as a helical bacterium, can generate a harmonic potential. How can one distinguish between an overall optical force and local optical forces acting on the structure?

The forces of an optical point trap on a spherical dielectric particle (a bead) are well understood in the meanwhile and have been described theoretically [18,19]. The theory, based on a separation of optical gradient and scattering forces, has also been extended to the trapping of single beads in line optical traps, i.e., by scanning a point trap very fast along a line [7,8]. In this work, we further extend the line trapping approach to an elongated helical bacterium, which is modeled as a chain of connected pearls.

Force on a small sphere. The force **F** of a static point trap at position $\mathbf{r}_L$ (L = laser focus) on an small spherical object at center position **a** can be calculated from the intensity of the incident and the scattered field, $\mathbf{E}_i(\mathbf{r}_L)$ and $\mathbf{E}_s(\mathbf{r}_L,\mathbf{a})$ according to Eq. (1).

$$\begin{aligned}\mathbf{F}(\mathbf{r}_L,\mathbf{a}) &= \mathbf{F}_{grad}(\mathbf{r}_L,\mathbf{a}) + \mathbf{F}_{scat}(\mathbf{r}_L,\mathbf{a}) \\ &= P(\mathbf{r}_L)\tfrac{1}{4}\mathrm{Re}\{\alpha\varepsilon\}\int \nabla\left|\mathbf{E}_i(\mathbf{r}-\mathbf{r}_L)+\mathbf{E}_s(\mathbf{r}-\mathbf{r}_L,\mathbf{a})\right|^2 s(\mathbf{r}-\mathbf{a})\,d^3r \qquad (1)\\ &\approx P(\mathbf{r}_L)\tfrac{\alpha n}{2c}\int \left(\nabla I_i\right)(\mathbf{r}-\mathbf{r}_L)\cdot s(\mathbf{r}-\mathbf{a})\,d^3r\end{aligned}$$

The optical force splits into two components: a gradient force $\mathbf{F}_{grad}$ pulling the object towards the focal center in all three directions and a scattering force $\mathbf{F}_{scat}$ (due to radiation pressure) pushing the object in axial direction. In consequence, the scattering force leads to a small axial offset of the stable trapping position (where $\mathbf{F}_{grad} = \mathbf{F}_{scat}$) and counteracts the gradient force. The ratio between both forces can be adjusted to a certain amount by over- or under-filling the BFP of the TL [16]. However, for small particles the scattering force is often negligibly small compared to the gradient force. The integral averages all intensity gradients inside the volume V of the scatterer [16] described by a shape function $s(\mathbf{r})$, which is $s(\mathbf{r}) = 1/V$ within the scatterer and $s(\mathbf{r}) = 0$ outside.

The scatterer is assumed to be non-absorbing and has a real polarizability α in a medium with a real electric permittivity $\varepsilon = n^2$. c/n the speed of light in the aqueous medium with refractive index $n \approx 1.34$.

#220691 - $15.00 USD Received 12 Aug 2014; revised 24 Sep 2014; accepted 25 Sep 2014; published 8 Oct 2014

$I_i(\mathbf{r}\text{-}\mathbf{r}_L)$ is the intensity at position $\mathbf{r}$ of the laser focus at position $\mathbf{r}_L = (r_x, r_y, r_z)$, such that the spatially confined intensity gradient is approximated by the derivative of a Gaussian function as shown in Eq. (2). The latter has focal widths $\Delta x \approx \Delta y \approx \frac{1}{2}\lambda/NA$, and $\Delta z \approx \lambda/(n\text{-}n\cdot\cos(\alpha))$ with $NA = n\cdot\sin(\alpha)$, corresponding to the full width half maximum of a diffraction limited focus:

$$\nabla I(\mathbf{r},\mathbf{r}_L) = I_0 \nabla_r \left(e^{-\left(\frac{x-x_L}{\Delta x}\right)^2} e^{-\left(\frac{y-y_L}{\Delta y}\right)^2} e^{-\left(\frac{z-z_L}{\Delta z}\right)^2} \right) \tag{2}$$

In Eq. (1) this intensity is further modulated by the dimensionless Gaussian distribution $P(r_L(t)) = P_0 \cdot \exp(-x_L^2(t)/\sigma_T^2)$ generated by the AOD in order to get a harmonic trap potential along the direction of the line trap with length L_T = 12 µm, too. (see Fig. 1(c)). $x_L(t)$ is the position of the laser in scan direction and σ_T = 4 µm represents the Gaussian width of the focus intensity distribution in time average. $I_0 \cdot P_0$ and σ_T determine the depth of the potential.

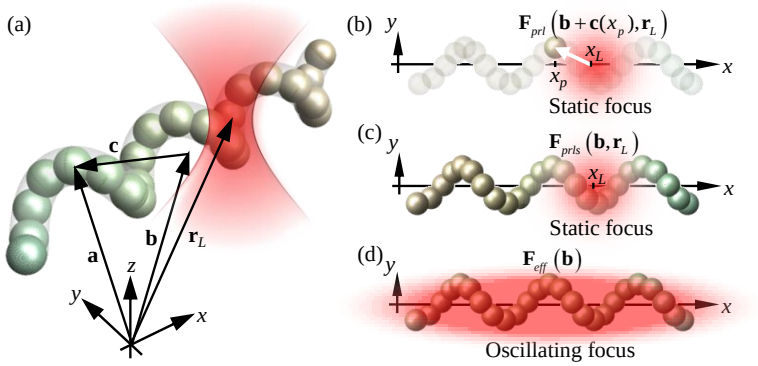

Fig. 2. Pearl model and principal of force generation. (a) The helical bacterium with center of mass position **b** is modeled as a chain of pearls at position **a** = **b** + **c**(x), where **c**(x) describes the slopes of the helix. The position of the laser focus is $\mathbf{r}_L$. (b)-(d) Illustration of the three steps to calculate the total force of the laterally sweeping focus on the whole bacterium.

Force on a thin helical structure. More precisely, we model the cell body as a chain of pearls or beads located at positions $\mathbf{a}(x) = \mathbf{b} + \mathbf{c}(x)$, where **b** is the center of mass position of the bacterium and Eq. (3) describes the helical slopes of the bacterium as illustrated by the inset of Fig. 1 and Fig. 2(a).

$$\mathbf{c}(x) = (x, R_H \cdot \cos(k_H x), R_H \cdot \sin(k_H x)) \tag{3}$$

$p = 1/k_H$ defines the periodicity of the helical structure of radius R_H. The diameter of such a pearl must be smaller than the narrowest extent of the laser focus, $\Delta x \approx \Delta y \approx \lambda/(2\,n)$, such that the Born approximation is valid. Therefore, the diameter of the cell tube d = 190 nm is a reasonable size of a pearl and $N = 2\Delta x / d$ = 4-5 pearls fit within a laser focus. However, for the ease of calculation and since a pearl has a low refractive index and a small d compared to the wavelength λ = 1064 nm, we consider the cell body to be a delta line: $s(\mathbf{r}\text{-}\mathbf{a}) = \delta(\mathbf{r}\text{-}\mathbf{a}(x))$.

$$\begin{aligned}
\mathbf{F}_{prl}(\mathbf{r}_L, \mathbf{a}(x)) &\approx \tfrac{\alpha n}{2c} P(\mathbf{r}_L) \int (\nabla I)(\mathbf{r}-\mathbf{r}_L) \cdot \delta(\mathbf{r}-\mathbf{a}(x)) d^3 r \\
&\approx \tfrac{\alpha n}{2c} P(\mathbf{r}_L) \cdot (\nabla I)(\mathbf{a}(x)-\mathbf{r}_L) \\
&= \tfrac{\alpha n}{2c} P(\mathbf{r}_L) \cdot (\nabla I) \begin{pmatrix} x + b_x - x_L \\ R_H \cos(k_H x) + b_y - y_L \\ R_H \sin(k_H x) + b_z - z_L \end{pmatrix}
\end{aligned} \tag{4}$$

#220691 - $15.00 USD Received 12 Aug 2014; revised 24 Sep 2014; accepted 25 Sep 2014; published 8 Oct 2014

The gradient force $\mathbf{F}_{prl}$ generated by the laser focus at position $\mathbf{r}_L = (x_L, 0, 0)$ on a single pearl is described by Eq. (4). In our model, we assume the individual pearls to be connected with each other through springs. Since we do not observe in the experiments that the trapped bacterium is squeezed together, we assume the springs to be stiff relative to the stiffness of the optical forces. Thus, the total force $\mathbf{F}_{prls}$ of a static laser focus on the illuminated part of the bacterium is obtained by integrating Eq. (4) over the lateral extent of the laser focus $2\Delta x$, leading to the summation of forces of N pearls in a center distance d to each other:

$$\begin{aligned}\mathbf{F}_{prls}(x_L,\mathbf{b}) &\approx \sum_{n=-N/2}^{N/2}\mathbf{F}_{prl}\left(x_L,\mathbf{b}+\mathbf{c}(x_L+n\cdot d)\right)\\ &\approx \tfrac{1}{d}\cdot\int_{x_L-\Delta x}^{x_L+\Delta x}\mathbf{F}_{prl}\left(x_L,\mathbf{b}+\mathbf{c}(x)\right)dx\end{aligned} \tag{5}$$

For a stiff connection of pearls, this expression describes the average center-of-mass force of a rod with length N·d within the laser focus. Optical torques are not considered here. Furthermore, the torsional friction of the long helical structure is too large to affect the movement of the rod during the scan period of the laser focus, which is $T_s = 1/f$ at a typical frequency f = 400 Hz. One- and two-dimensional force profiles $\mathbf{F}_{prls}(\mathbf{r}_L)$ on the helical bacterium for various positions $\mathbf{r}_L$ of a laser focus are shown in Fig. 3 as a result of the numerical evaluation of Eq. (5).

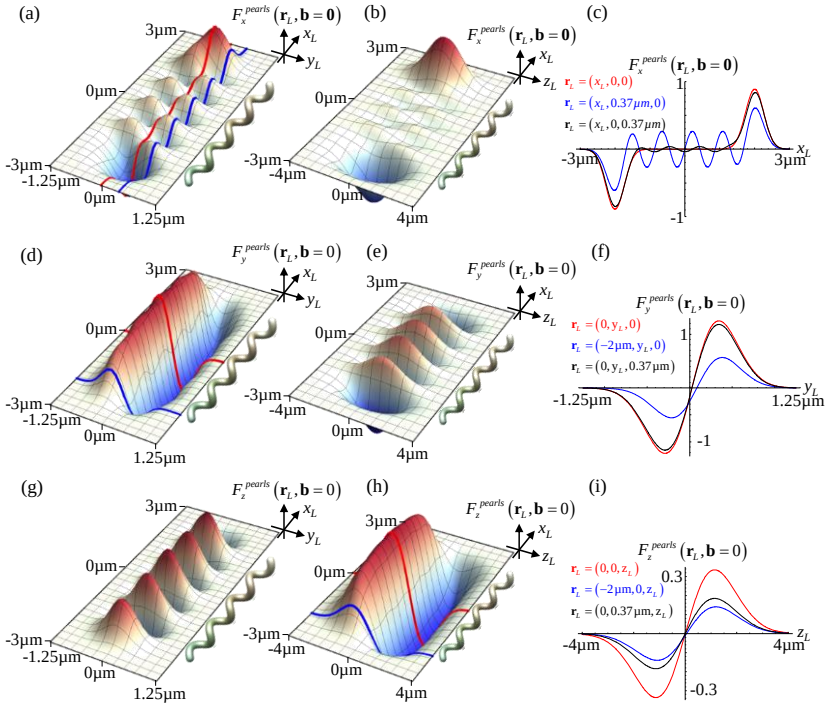

Fig. 3. Calculated force profiles $\mathbf{F}^{prls}(\mathbf{r}_L)$ on a helical structure. The laser focus is scanned along the position $\mathbf{r}_L$ and is modulated in intensity over the width $\sigma_T = 4\ \mu m$. The helical structure is centered at $\mathbf{b} = \mathbf{0}$. (a), (b) Force profiles of $\mathbf{F}_x^{prls}$ in x-y and x-z direction. Force amplitudes are for Figs. (a) and (b) ± 0.9 a.u. (arbitrary units). (c) Line scans as indicated in (a). (d), (e) Force profiles of $\mathbf{F}_y^{prls}$ in the x-y and x-z plane. Force amplitudes are for Fig. (d) –1.3/1.3 a.u. and Fig. (e) –0.4/0.4 a.u.. (f) Line scans as indicated in (d). (g), (h) Force profiles of $\mathbf{F}_z^{prls}$ in the x-y and y-z plane. Force amplitudes are for Fig. (g) –0.015/0.015 a.u. and Fig. (h) –0.36/0.36 a.u. (i) Line scans as indicated in (g). Color scales range from negative (blue to positive (red) values.

As explained at the beginning, an object-adapted optical trap distributes the optical energy smoothly across the extent of the object. Therefore, the laser focus is laterally swept across

#220691 - $15.00 USD Received 12 Aug 2014; revised 24 Sep 2014; accepted 25 Sep 2014; published 8 Oct 2014

the object. This leads to a time averaged optical force $\mathbf{F}_{opt}(\mathbf{b}) = \langle \mathbf{F}_{prls}(x_L(t), \mathbf{b}) \rangle$ on the total bacterium, which we expect to be linear restoring for displacements $\mathbf{b}$ of the bacterium. Hence, Eq. (5) has to be integrated over all focus positions $0 \le x_L = v_L t \le L_T = v_L T_s/2$.

$$\begin{aligned} \mathbf{F}_{opt}(\mathbf{b}) &= \tfrac{2}{T_s}\int_0^{T_s/2} \mathbf{F}_{prls}\left(v_L \cdot t, \mathbf{b}\right) dt \\ &= -\left(\kappa_{xe} \cdot b_x, \kappa_{ye} \cdot b_y, \kappa_{ze} \cdot b_z\right) = -\ddot{\boldsymbol{\kappa}}_{eff} \cdot \mathbf{b} \end{aligned} \tag{6}$$

The diagonal matrix $\ddot{\boldsymbol{\kappa}}_{eff}$ describes the effective (time averaged) stiffness κ_{xe}, κ_{ye} and κ_{ze}, of the object adapted optical trap. The numerical solution of Eq. (6) is plotted in Fig. 4 for all three spatial directions and different center positions $\mathbf{b}$ of the bacterium. In the experiments, the center-of-mass (COM) displacements $\mathbf{b}$ can be reached by the bacterium either actively or by diffusion.

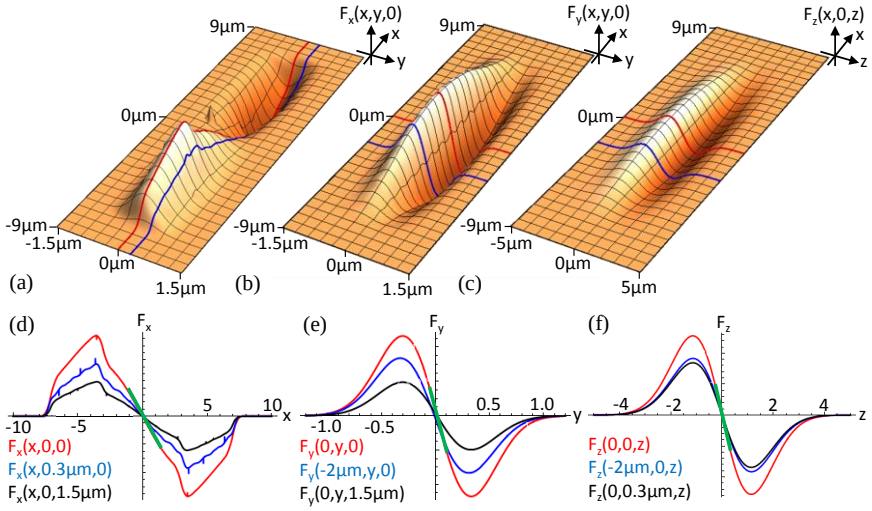

Fig. 4. Calculated force profiles $(\mathbf{F})_{opt}(\mathbf{b})$. (a)–(c) Simulated force profiles for the center of mass position $\mathbf{b}$ of the bacterium inside a line trap for all three directions. (d)–(f) Line scans as indicated in Figs. (a)–(c). The green lines illustrate the linear force dependence for small displacements from the trap center. Numbers on the abscissae are in µm. (Reproduced from supplementary information of [14])

At this point it is important to inspect the line profiles in Figs. 4(d)–4(f), where it can be clearly seen that the optical force is linear for small displacements from the center of the line trap, i.e., for small positions $\mathbf{b}$ relative to the center of the trap. Therefore, the approximation of a linear restoring force $-\kappa_i \cdot b_i$ (i = x,y,z) according to the second line in Eq. (6) is valid.

To theoretically estimate the force constants, we use a first order approximation of Eq. (4) which results in trap stiffness $\boldsymbol{\kappa}_{prl} = (\kappa_{x,prl}, \kappa_{y,prl}, \kappa_{z,prl})$ of a single pearl: $\boldsymbol{\kappa}_{prl} = n_m \alpha I_0/c\ (1/\Delta x^2, 1/\Delta y^2, 1/\Delta z^2) = (1.13, 1.13, 0.17)$pN/µm. Here, we used the Claussius-Mossotti relation $\alpha = 3V(m^2\text{-}1)/(m^2 + 1)$, $m = n_s/n_m$, with $n_s \approx 1.4$ which is a reasonable value for the outer part of many cells, the volume V of a pearl with diameter $d_t = 0.2$ µm and $I_0 = P_0/\pi\Delta x^2$ with $P_0 = 180$ mW. Since the force $\mathbf{F}_{prls}$ on all pearls inside the focus is the sum of $N \sim 4$ pearls with force of $\mathbf{F}_{prl}$, the forces constant $\boldsymbol{\kappa}_{prls}$ of $\mathbf{F}_{prls}$ also increases by the factor N: $\boldsymbol{\kappa}_{prls} = 4 \cdot \boldsymbol{\kappa}_{prl}$. The effective force constants $\boldsymbol{\kappa}_{eff}$ of the line trap are reduced by $\Delta A = \pi\Delta x^2 / 2\Delta x L_T = 1/15$ since the laser power P_0 is distributed over a larger area $2\Delta x L_T$ instead of $\pi\Delta x^2$. Additionally, the stiffness in scan direction is given by the modulation width $\sigma_T \approx 4$µm $> \Delta x$. This results in a secondary decrease by a factor $\Delta x/\sigma_T = 0.18$ in scan direction. Taken together, we theoretically estimate the effective force constants $\boldsymbol{\kappa}_{eff} = 4/15\ (0.18\kappa_{x,prl}, \kappa_{y,prl}, \kappa_{z,prl}) = (0.041, 0.300, 0.045)$ pN/µm. As shown in section 5, this agrees reasonably with the experimentally obtained values: $\boldsymbol{\kappa}_{eff,exp}$

#220691 - $15.00 USD Received 12 Aug 2014; revised 24 Sep 2014; accepted 25 Sep 2014; published 8 Oct 2014

= (0.016, 0.390, 0.038) pN/µm. However, the amplitudes of the simulated force profiles (Fig. 3 and Fig. 4) are given in a.u. (arbitrary units) since this is only an estimation.

In addition to the force profiles, the effective trapping potential $V_{eff}(\mathbf{b})$ are calculated numerically as shown in Fig. 5 for different situations. We applied parabolic fit functions to the line profiles in Figs. 5(d)–5(f) in order to show that the potential is harmonic for small displacements in all three directions as indicated by Eq. (7). Again, the Gaussian intensity modulation $P(t)$ determines the harmonic potential along the scan direction x.

$$V_{opt}(\mathbf{b}) = -\int_{-\infty}^{\mathbf{b}} \mathbf{F}_{opt}(\mathbf{r})\, d\mathbf{r} \approx \tfrac{1}{2}\kappa_{xe}\cdot b_x^2 + \tfrac{1}{2}\kappa_{ye}\cdot b_y^2 + \tfrac{1}{2}\kappa_{ze}\cdot b_z^2 \qquad (7)$$

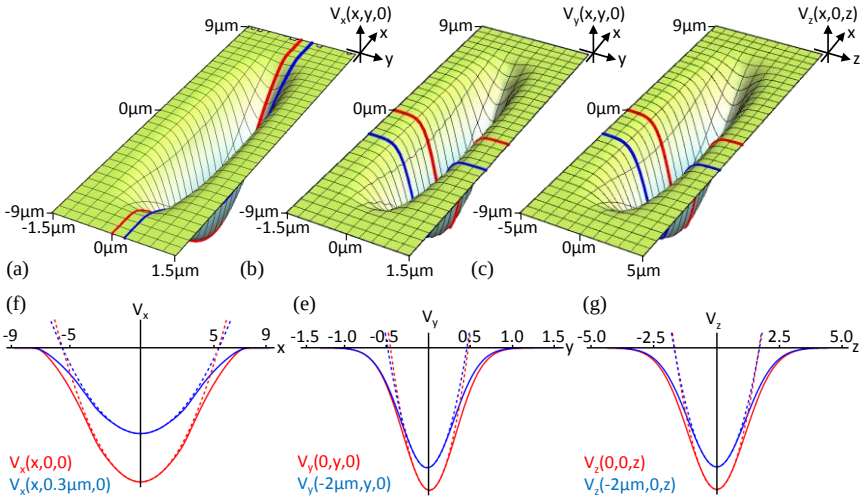

Fig. 5. Calculated optical potentials $V_{opt}(\mathbf{b})$. (a)–(c) Simulated potential profiles for the center of mass position **b** of the bacterium inside a line trap for all three directions. (d)–(f) Line scans (solid) as indicated in figures (a)-(c) and parabolic fits (dashed). Numbers on the abscissae are in µm. (Reproduced from supplementary information of [14])

4. Interferometric shape tracking of an asymmetric structure

The interferometric shape tracking technique allows acquiring 3-D images of the bacterium at a rate up to 1000 Hz (depending on the scan rate of the laser focus). The resulting images have a much higher contrast and resolution compared to other imaging methods applicable to the helical bacterium. This section is meant to summarize the main ideas and to provide the necessary background for section 5.

The technique is an extension to the successful back focal plane tracking used for beads. The method exploits the position dependent interference pattern of the field $\mathbf{E}_s$ scattered at the trapped cell body element, i.e., a few pearls, with the unscattered light $\mathbf{E}_i$. The phase $\varphi_s(\mathbf{c})$ of the scattered light strongly depends on the position $\mathbf{c}(t, x_L)$ of the cell body element relative to the position x_L of the optical trap, i.e., the center of the focus. Therefore, any change of the phase difference between both fields related to a position change of the scatterer results in a change of the interference pattern. This change can be measured very sensitively by a QPD, therewith tracking the position of the scatterer [14].

The interference intensity $\tilde{I}(\mathbf{k},\mathbf{c}) = c\varepsilon_0 \left|\tilde{\mathbf{E}}_i(\mathbf{k}) + \tilde{\mathbf{E}}_s(\mathbf{k},\mathbf{c})\right|^2$ in the back focal plane of the detection lens (Fourier space) with coordinates $\mathbf{k} = (k_x, k_y)$ is integrated over the area of each quadrant A_n of the QPD ($n = 1, \ldots, 4$). The raw signal of the n-th quadrant is given by Eq. (8):

#220691 - $15.00 USD Received 12 Aug 2014; revised 24 Sep 2014; accepted 25 Sep 2014; published 8 Oct 2014

$$\begin{aligned}\hat{S}_n^{raw}(\mathbf{c}) &= P(t)\iint_{A_n}\left(\left|\tilde{\mathbf{E}}_i(\mathbf{k})\right|^2+\left|\tilde{\mathbf{E}}_s(\mathbf{k},\mathbf{c})\right|^2+2\,\mathrm{Re}\left\{\tilde{\mathbf{E}}_i(\mathbf{k})\cdot\tilde{\mathbf{E}}_s^*(\mathbf{k},\mathbf{c})\right\}\right)d^2k \\ &\approx 2A\cdot\iint_{A_n}\Delta\varphi_s(\mathbf{k},\mathbf{c})\,d^2k+S_{off,n}(t)\end{aligned} \tag{8}$$

$P(\mathbf{r}_L(t))$ is the dimensionless Gaussian intensity modulation also generating a harmonic potential in scan direction. However, for tracking of the bacterial shapes $P(t)$ can be approximated to be constant over the extent of the bacterium, since the cell is much shorter (L_H = 3-5 µm) than the whole line trap (L_T = 10-12 µm) and $\sigma_T \approx L_T/2$, i.e., $P(L_H/2) \approx 0.9$ (also see Fig. 1 inset).

The measured raw signal is composed of a signal offset $S_{off,n}(t)$, which is recorded without scatterer and can be easily subtracted from the raw signal. The remaining term represents the area integral over the interference term, which can be simplified as shown in Eq. (9):

$$\begin{aligned}\mathrm{Re}\left\{\tilde{\mathbf{E}}_i\cdot\tilde{\mathbf{E}}_s^*(\mathbf{c})\right\} &\approx \tfrac{1}{2}\left|\tilde{\mathbf{E}}_i+\tilde{\mathbf{E}}_s(\mathbf{c})\right|^2-\tfrac{1}{2}\left|\tilde{\mathbf{E}}_i\right|^2 \\ &= \left|\tilde{\mathbf{E}}_i\right|\cdot\left|\tilde{\mathbf{E}}_s^*(\mathbf{c})\right|\cdot\mathrm{Re}\left\{\exp\left(i\varphi_s-i\varphi_i(\mathbf{c})\right)\right\} \\ &\approx A\cdot\sin\left(\Delta\varphi_s(\mathbf{c})\right)\approx A\cdot\Delta\varphi_s(\mathbf{c})\end{aligned} \tag{9}$$

The term $A = 2\left|\tilde{\mathbf{E}}_i\right|\cdot\left|\tilde{\mathbf{E}}_s^*(\mathbf{c})\right| \approx$const. is approximately constant for small displacements $c_y < \tfrac{1}{2}\Delta y$ and $c_z < \tfrac{1}{2}\Delta z$. The phase difference $\varphi_s(\mathbf{c}) - \varphi_i = (\varphi_i + \pi/2 + \phi_s) - \varphi_i = \phi_s + \pi/2$ contains the $\pi/2$ phase delay of the Rayleigh-scattered field relative to the incident. A lateral displacement in the focal plane leads to a tilt of the scattered light in the back focal plane of the detection lens ($\mathbf{E}(x-c_x)\rightarrow\tilde{\mathbf{E}}(k_x)\exp(ik_xc_x)$) and therewith results in a linear dependence of phase and displacement $\phi_s(c_x, c_y) = k_xc_x + k_yc_y$ for small $|\mathbf{c}|$. The linear dependence between the phase $\phi_s(c_z) \approx -a\cdot k_zc_z$ and the displacement c_z is also obtained in in axial direction, when the Gouy phase anomaly of the focused trapping beam $\varphi_i(z) = k_zz - \tan^{-1}(k_0/n\,NA^2\,z)$ is considered [14].

Using $\phi_s(\mathbf{c}) = k_xc_x + k_yc_y - ak_zc_z$ and inserting the term of Eq. (3), the shape tracking signal for a laser at position x_L can be well approximated to the following expression $S(\mathbf{c}) = \hat{S}_n^{raw}(\mathbf{c}) - \hat{S}_{off,n}(\mathbf{c})$:

$$\begin{aligned}S(\mathbf{c}(x_L)) &\sim \iint\left(k_xx_L+k_yR_H\cos(k_Hx_L)-ak_zR_H\sin(k_Hx_L)\right)\mathbf{H}\,d^2k \\ &\approx\left(g_x\cdot x_L,\quad g_y\cdot R_H\cos\left(k_Hx_L\right)/q_y,\quad g_z\cdot R_H\sin\left(k_Hx_L\right)/q_z\right)\end{aligned} \tag{10}$$

The vector operator $\mathbf{H}(\mathbf{k})$ generates the difference between the signals of the vertical and horizontal two quadrants for the lateral position signals and takes the sum of all four quadrants for the axial position signal [14].

The linear approximation in the second line of Eq. (10) holds for small displacements from the trap center. The constants g_i ($i = x, y, z$) are the detector sensitivities, which have to be determined through a calibration procedure explained in the next paragraph. In contrast to conventional BFP-tracking of beads, we have to further consider the correction factors $q_y > 1$ and $q_z > 1$. These factors are due to the helical slope of the cell and are explained in sections 5 and 6, together with κ_i and g_i.

#220691 - $15.00 USD Received 12 Aug 2014; revised 24 Sep 2014; accepted 25 Sep 2014; published 8 Oct 2014

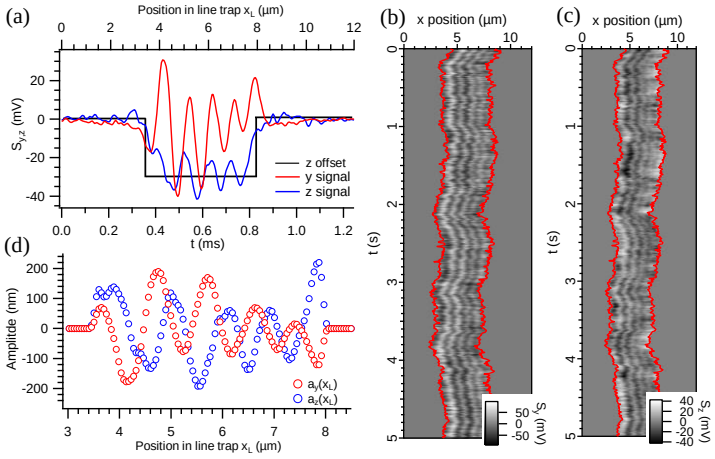

Fig. 6. Measured QPD signals from the helical bacterium. (a) y- and z- signals (according to Eq. (10)) over time (bottom axis) and corresponding position inside the line trap (top axis). (b) Kymographs of y-signal. The red lines show the edges of the cell. (c) Kymographs of z-signal. (d) Slightly smoothed slope amplitudes $a_y(x_L)$, $a_z(x_L)$ obtained from a) after calibration. The rectangular offset function of the axial (z) signal has been removed.

The signals recorded by the shape tracking method are shown for a single focus scan in Fig. 6(a)). The signal scale is in Volt for the raw signals according to Eq. (10). A calibrated version of the same data is shown in Fig. 6(d) (see next section for calibration). Figures 6(b) and 6(c) show Kymographs (i.e., the temporal evolution of single line scans) of S_y and S_z of a dead bacterium, illustrating thermal fluctuations of the cell inside the trap. It should be noted that the shape of a dead cell remains the same as for a living specimen (within the time window we analyzed the cells). Cells typically die after being trapped for 30-60 s due to the formation of reactive oxygen species (ROS) caused by the high laser power of ~180 mW in the focal plane. While this can be used to calibrate traps, oxygen scavenging enzymes such as catalase and glucose oxidase can be also used to scavenge the ROS molecules and to keep cells alive for more than 10 minutes.

Data of living and actively self-propelling cells as well as 3D movie reconstructions can be found in [14].

5. Detector and trap calibration for an asymmetric structure

An elegant way to calibrate an optical trap, i.e., to find the trap and detector sensitivities κ_j and g_j ($j = x,y,z$), is the so called Langevin method [19,20]. In general, by solving the equation of motion for a highly over damped particle in an external harmonic potential, an exponential decay of the autocorrelation (AC) function of the particle trajectory is found. The autocorrelation time is given by $\tau = \gamma / \kappa$. If the friction coefficient γ is known, e.g. $\gamma = 6\,\pi R\eta$ for a spherical bead with radius R in a fluid with viscosity η, the trap sensitivity κ can be calculated by fitting the exponential slope of the AC. Further, the general definition of the detector sensitivity $g_j = S_j / c_j$ is the proportionality between the signal from the detector (in Volt) and the true bead position (in meter). An equivalent definition is the relation between signal fluctuation width $\sigma_j' = \langle \Delta S_j \rangle$ and particle fluctuation width $\sigma_j = \langle \Delta b_j \rangle$, i.e., $g_j = \sigma_j' / \sigma_j$. In this representation, the equipartition theorem $\frac{1}{2}\,\kappa_j\,\sigma_j^2 = \frac{1}{2}\,k_B T$, which links the particle fluctuations with the thermal energy, can be used to determine g_j. The signal fluctuation width can be found by fitting a Gaussian function to the signal histogram.

However, the Langevin calibration method relies on the knowledge of the friction coefficient γ, which is unknown for a helically formed tube with a variable diameter, pitch and overall length. Some publications use the coefficients for a straight cylinder instead, which does not lead to correct results in our case. Therefore we go a different way and perform a detector calibration scan over a freely diffusing helical bacterium to determine g_y

#220691 - $15.00 USD Received 12 Aug 2014; revised 24 Sep 2014; accepted 25 Sep 2014; published 8 Oct 2014

and therewith κ_y and γ_y. This approach is similar to scanning a bead through the laser focus which is often used to calibrate optical traps.

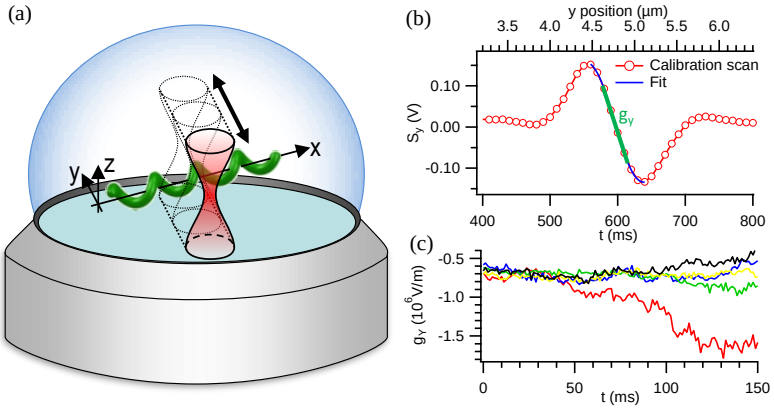

Fig. 7. Detector calibration at a freely diffusing cell. (a) Calibration schematic. The trap direction is suddenly changed by 90°, therefore performing a 'calibration scan' perpendicular to the long axis of the cell. (b) QPD signal S_y of the calibration scan showing the unique (blue fit) and linear (green line) detection region with gradient g_y. (c) Temporal behavior of g_y for five different calibration scans (indicated by different colors).

The calibration scan is illustrated in Fig. 7(a). Initially, the cell is stably held by the line trap along x. The scan direction of the laser focus is suddenly changed by 90°, thus scanning in y direction, i.e., perpendicular to the long axis of the cell. The corresponding signal is shown in Fig. 7(b) for a single focus scan. Since the position of the laser is known at every time, the signal amplitude $S_y(y)$ can be mapped to a certain displacement y of the laser from the center of the cell body ($S_y(b_y) = 0V$) and thus $g_y = \partial/\partial y\ S_y(0)$ can be determined as indicated by the slope of the green line.

Since the cell is no longer stably trapped during the calibration scan, one needs to check the stability and reliability of this method because now the cell can rotate or move out of its initial position. Thus we performed the calibration scan over some hundreds of milliseconds with a scan rate of 400 Hz and analyzed the temporal changes of g_y. The result is shown in Fig. 7(c) for five different scans. The detector sensitivity stays remarkably constant over the first 50 ms. Secondly, different calibration scans (at different cell positions) result in the same value for g_y within a deviation of ~10%. Therefore, the value for g_y can be further improved by taking the mean value of the first 50 ms (= 40 scans) of a calibration scan.

As already mentioned, g_y with correction factor $q_y > 1$can now be used together with the equipartition theorem to determine κ_y and γ_y

$$\kappa_y = \frac{k_B T \cdot g_y^2}{\sigma_y'^2 \cdot q_y^2} \qquad \gamma_y = \tau_y \kappa_y \tag{11}$$

To calibrate in axial direction, we use the symmetry property of the cell along its long axis, which means that the cell has equal friction coefficients in y- and z-direction

$$\gamma_y = \gamma_z \quad \Rightarrow \quad \kappa_z = \frac{\gamma_y}{\tau_z} \qquad g_z = q_z \sigma_z' \sqrt{\frac{\kappa_z}{k_B T}} \tag{12}$$

The calibration in scan direction is much easier since the position of the laser, and therefore the position of the cell in scan direction, is known

#220691 - $15.00 USD Received 12 Aug 2014; revised 24 Sep 2014; accepted 25 Sep 2014; published 8 Oct 2014

$$\kappa_{xe} = \frac{k_B T}{\sigma_x^2} \qquad \gamma_x = \tau_x \kappa_x \tag{13}$$

Equations (11)–(13) show how the calibration constants can be determined ideally from the position signals. However, the method relies on center of mass positions (CMP) representing the whole object in order to calculate position histograms and autocorrelations. Regarding the typical case of a bead in a point trap, the detector signals S_i ($i = x, y, z$) directly represent the CMP position. For the line-trapped helix, they have to be extracted from the signals S_i in order to determine the parameters σ_j and τ_j, first. In scan direction, this is done by a slightly extended version of the build-in edge detection algorithm of our analysis software (Wavemetrics Igor Pro). The algorithm detects the beginning (left edge = LE) and end (right edge = RE) of the cell for every scan in a kymograph shown in Figs. 6(b) and 6(c) (red lines show the borders/edges of the cell). The edge detection result is also shown in Fig. 8(a) with a corresponding histogram of the left edge (as representative) in Fig. 8(d) and autocorrelation in Fig. 8(g).

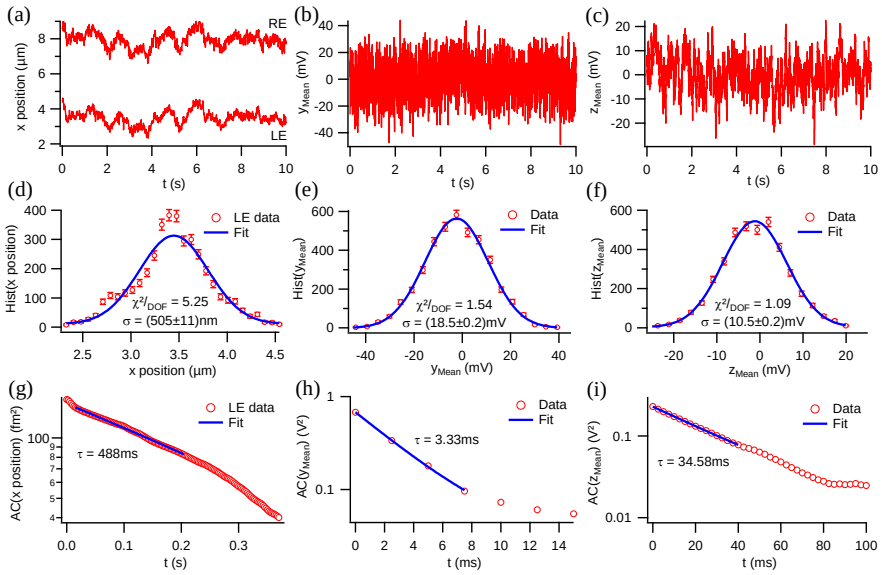

Fig. 8. Trap calibration for a helical structure. (a) Position trajectory of the cell's left and right edge (LE and RE) (b) and (c) Trajectory of the cell's center of mass position (CMP) in y- and z- direction. (d) – (f) Histograms (Hist) of corresponding position data with error bars indicating the standard deviation $1/\sqrt{N}$. Gaussian fits in blue. (g) – (i) Autocorrelations (AC) of corresponding position data and fit of exponential decay (y axis log scaled).

In y- and z-direction, the CMP is equal to the arithmetic mean of S_y and S_z between the left and right edge of the cell as shown in Figs. 8(b) and 8(c). Histograms of the corresponding CMP values are shown in Figs. 8(e) and 8(f) and ACs in Figs. 8(h) and 8(i). As one can already see from the fits to the ACs, the trapping stiffness κ is the strongest in y direction and the weakest in scan direction since the autocorrelation times are $\tau_y < \tau_z < \tau_x$.

The calibrated slopes of a representative scan of the helical cell are already shown in Fig. 6(d). Here, the CMP value has been subtracted as an offset to show the similar amplitudes in y and z direction. One can also clearly see the $\pi/2$ phase shift between both directions resulting from the dependence of $\mathbf{c}(x)$ on *cos* and *sin* functions. The helical pitch p is found for various measurements to be in the range of 900 µm to 1000 µm, which fits well to detailed analyses made by Trachtenberg & Gilad [13] and justifies the assumption of stiff inter-connecting springs in section 3.

#220691 - $15.00 USD Received 12 Aug 2014; revised 24 Sep 2014; accepted 25 Sep 2014; published 8 Oct 2014

Results of the calibration are given below for one representative cell/scan out of several - at a laser power $I_0 \approx 180$ mW. Indeed, we did scan a couple of cells all leading to comparable results. $g_y/q_y = (-179 \pm 2)\text{kV}\cdot\text{m}^{-1}$, $g_z/q_z = (-81 \pm 2)\text{kV}\cdot\text{m}^{-1}$, $\kappa_x = (0.016 \pm 0.001)\text{pN}\cdot\mu\text{m}^{-1}$, $\kappa_y = (0.39 \pm 0.04)\text{pN}\cdot\mu\text{m}^{-1}$, $\kappa_z = (0.038 \pm 0.003)\text{pN}\cdot\mu\text{m}^{-1}$, $\gamma_x = (8.0 \pm 0.4)\text{fN}\cdot\text{s}\cdot\mu\text{m}^{-1}$, $\gamma_{y,z} = (1.3 \pm 0.1)\text{fN}\cdot\text{s}\cdot\mu\text{m}^{-1}$.

The estimation of the correction factors $q_y = 4.0$ and $q_z = 1 / 1.5$ is explained in the next section. At this point, it should be noted that the experimentally obtained drag coefficients γ_x and $\gamma_{y,z}$ deviate from those of a cylinder with a corresponding length $L_C = 4$ µm and diameter $D_C = 2R_H + d = 560$ nm: $\gamma_{C,x} = 14.2\text{fN}\cdot\text{s}\cdot\mu\text{m}^{-1}$ and $\gamma_{C\,y,z} = 17.9\text{fN}\cdot\text{s}\cdot\mu\text{m}^{-1}$.

Estimation of the axial tracking range. In BFP-interferometry, the tracking range is limited by a unique detection region (UDR, also see Fig. 7). The width of this range depends mainly on the NA of the trapping lens (TL) [16], the object size and the refractive index but hardly on the detection NA. By moving an object axially through the trapping focus, the stable axial trapping position inside the UDR can be estimated. In bead assays, this is done after sticking the bead to the coverslip by adding salt to the trapping medium. The coverslip can then be moved stepwise through the focus with the help of a piezo and the detection signal can be recorded. The resulting slope resembles a sinus function between $-\pi$ and π, i.e., the signal has a clear minimum and a maximum limiting the unique detection region. Comparing to the mean position signal of the bead diffusing inside the trap, the trapping position relative to the positions of the minimum and maximum detection signal can be determined.

This method was applied to a horizontally trapped bacterium, since we were not able to stably attach the cell to the cover slip. We therefore just pushed the cell out of the trap by moving the piezo from below the cell towards the trap as illustrated in Figs. 9(a)–9(c). We plotted the maximum of every line scan during this experiment vs. the current piezo position (Fig. 9(d)) resulting in a trapping position (point B) of ~800 nm below the maximum detection signal (point C). Comparing this to measurements with beads for identical optical parameters [16], this indicates that the cell is trapped only ~150 nm (or 8% of full UDR) above the geometrical center of the focus. Thus, the scattering force (which mainly pushes the cell in axial direction) is small relative to the gradient force as we assumed in section 3 to calculate the trapping forces and potentials. Instead of taking the maximum per line scan, one may take the mean value of every line, which does not change the result.

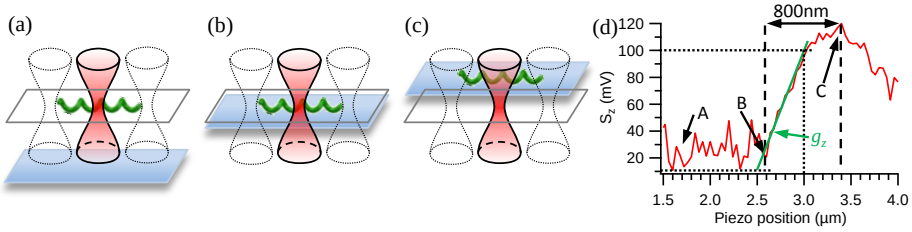

Fig. 9. Sedimentation experiment to estimate the tracking range. (a) The bacterium is trapped far away from the cover slip (blue rectangle) in the focal plane (grey rectangle) of the TL. (b) The cover slip is moved towards the cell until they touch. (c) The cover slip is moved further thus pushing the cell out of the trap. (d) Maximum value per line scan of axial QPD signal S_z at every piezo position.

Similar to the detection scan shown in Fig. 7, the detector sensitivity $g_z / q_z \approx$(90 mV / 500 nm) / 1.5 = 1 20 kV/m (in z-direction) can be determined from the signal gradient when the cell is pushed out of the trap as indicated in Fig. 9. This value is a factor 1.5 larger than the value shown further above and obtained by our calibration technique, however, the parameters of the line-trap (scan frequency f = 200 Hz, trap length L = 10 µm, modulation width σ_T = 5 µm) were different during both experiments. Therefore, we find that both values agree quiet well.

#220691 - $15.00 USD Received 12 Aug 2014; revised 24 Sep 2014; accepted 25 Sep 2014; published 8 Oct 2014

6. Signal averaging inside a diffraction limited focus

As pointed out in section 4, the aforementioned calibration procedure results in diameters of the helical cell body which are smaller than the true cell diameter. The relation between the actual diameter D and the apparent diameter D_y' is $q_y = D/D_y'$, or $q_z = D/D_z'$, correspondingly. The occurrence of the factors q_y and q_z is purely geometrical and can be explained by our pearl model. A quantitative estimation is possible by simulations of the bacterium's 2D interferometric tracking signal. Since the wavelength in the trapping medium $\lambda = \lambda_0/n_m$ = 800 nm is in the range of the projected length of one helical winding $p \approx 900$nm, the positions of several pearls are averaged at every focal position during a scan. This is illustrated in Fig. 10(a), where all position signals of the green pearls of the cell body are averaged within the laser focus corresponding to the signal of a virtual pearl (shown in blue). Apparently, the position $D_y'/2$ of this blue pearl is smaller than the true position $D/2$ of the cell body.

The different q-factors in lateral and axial direction result from the different focus widths in both directions, for which we estimate $\Delta z/\Delta y = \frac{1}{2}\cdot\sin\alpha/(1-\cos\alpha) = 2.6$ (according to the theoretical resolution limit). The averaging effect is therefore less pronounced in the z-direction requiring a smaller correction factor q_z. One can estimate for the ratio of both apparent diameters $D_y'/D_z' = q_y/q_z = \Delta z/\Delta y = 2.6$, such that $q_z = q_y / 2.6 \approx 1.5$

However, there is a second calibration scheme (referred to as 'method 2') that can be used. It is illustrated in Fig. 10(b), where the cell is stably trapped in a line trap while a second trap rapidly scans a meander-like trajectory. This resembles many subsequent calibration scans, each slightly displaced in direction of the long axis of the cell. Parameters like the minimum signal value of every such calibration scan (as well as the zero crossing point or the maximum) should follow the sinusoidal geometry of the cell, thus giving another way to estimate the cell diameter D. Figure 10(c) shows simulated 2D interferometric signals of such a meander scan over a fixed cell (no thermal motion). The green line indicates the first calibration method, i.e., only one scan perpendicular to the cell body resulting in the detector sensitivity g_y. The red line indicates method 2, where the zero crossing point of every scan perpendicular to the cell body of a 3 µm long meander scan is shown. The amplitude of this sinusoidal red line resembles the helical amplitude D_y'.

Experimentally, method 2 is more difficult to realize than method 1 and needs two traps which are steerable independently from each other. We achieved this by superposing the zeroth orders (steered by Galvanometric mirrors for the meander scan) and the first orders (AOD beam, used for the line trap) of both AODs as described in chapter 1. Both beams are polarized perpendicular to each other in order to separate them for an independent tracking. The subsequent meander scans are performed on the same area of 3 µm x 10 µm (x, y) and a discretization of 100 nm resulting in ~9 scans per helical winding. Figure 10(e) shows three individual meander scans separated by the white/black dashed lines (note that only the area of subsequent 3 µm x 2.5 µm scans are shown and that the scale of the vertical axis is continuously although individual scans span only 3 µm in that direction).

The position of the signal minimum (minpos) of each scan is shown in Fig. 10(f). Since the slope of minpos should resemble the sinusoidal form of the helix, we fit minpos accordingly (blue lines). Brownian motion of the cell is suppressed by the line trap, however, some scans are distorted too heavy and the fit result is poor. We filtered these events with the spatial frequency $0.82\ \mu m^{-1} \le k_H = 1/p \le 1.16 \mu m^{-1}$ of the cell (obtained by a PSD to minpos - see Fig. 10(g) which is one of the fit parameters, too. (fit results for p are shown in Fig. 10(h) with the filter interval as grey box). After applying the filter, we obtain 9 out of 64 scans where the sinusoidal fit matches the spatial frequency of the cell nicely. The corresponding cell diameters (twice the amplitude of the fit) are shown in Fig. 10(i) together with the mean diameter of the cell $D'_{Mean} = (95.5 \pm 4.5)$ nm.

To check if there is any systematic relation between the factors q_y, q_z, p and D, we used the Gaussian beam model [21,22] to simulate the interferometric QPD signals for various cell diameters and helical pitches. We plotted the ratio q_y for p = 900 nm for both methods as shown in Fig. 10(d), to see if the simulations can explain the experimental results. With

#220691 - $15.00 USD Received 12 Aug 2014; revised 24 Sep 2014; accepted 25 Sep 2014; published 8 Oct 2014

method 1, we experimentally found an apparent mean diameter D' = 57 nm for the representative scan in section 5. According to the simulations this is equivalent to q_y = 4.0 or D = 230 nm. For method 2, we found D = 330 nm and q_y = 3.3 (for a different cell). The distribution for D from [13] results in a mean value for the actual cell diameter D_T = 360 nm with a standard deviation σ_{DT} = 90 nm as indicated by the grey shaded Gaussian distribution in Fig. 10(d). Although both values D_1 and D_2 tend to be smaller than D_T, the result for D_2 is in the range of one standard deviation whereas D_1 differs by only $1.4\sigma_{DT}$. Thus, the results of both methods together with the correction factors derived by simulations are in good agreement with values obtained by complementary techniques.

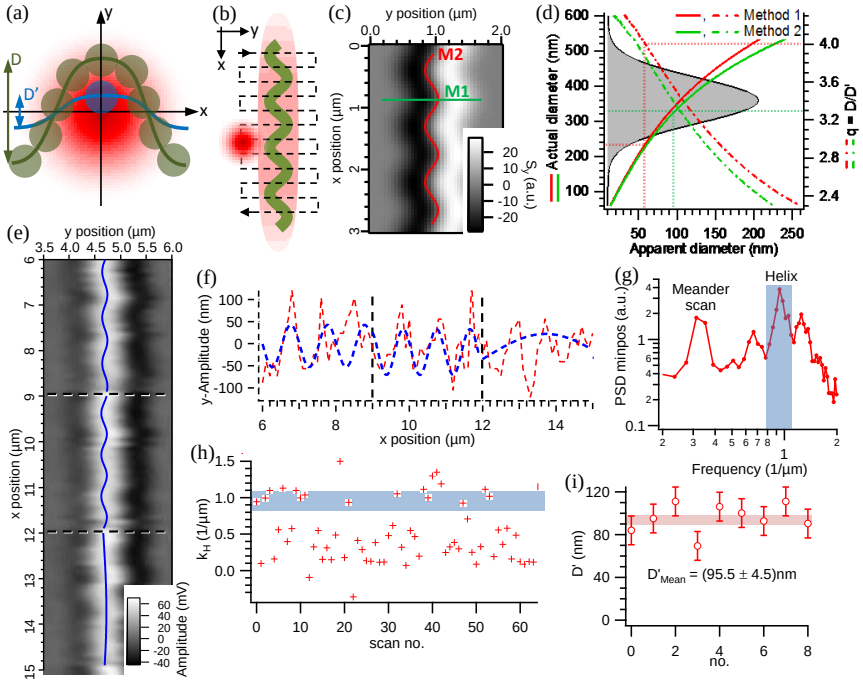

Fig. 10. Analysis of tracking signals from focal averaging. (a) Illustration of focal averaging due to the extended helical structure with diameter D inside a point focus. (b) Meander scan scheme, comparable to multiple subsequent calibrations scans. (c) Simulated meander scan of a helical structure with indicated calibration scans by method M1 and M2. (d) Ratio $q_y = D/D_y'$ of the actual cell diameter D and the apparent diameter D_y' retrieved from the simulation for p = 900 nm. Dashed lines indicate experimentally obtained q values. The grey shaded area represents the Gaussian distribution of D from [13]. (e) Subsequent experimental meander scans with a length of 3 µm each. (f) Positions of the signal minima (min pos) of every line scan and sinusoidal fits. (g) Power spectral density (PSD) of minpos clearly showing the frequency of the meander scan (f = 0.33 µm^{-1}) and the helix itself (f = (0.94 ± 1.2) µm^{-1}, grey box). (h) Results for the frequency fit value and allowed frequency band (grey box, same as in h). (i) Diameter D_y' after filtering for allowed values. Error bars represent the standard deviation of a single value. The mean diameter and its standard deviation are indicated (light red box).

7. Summary and conclusions

Optical trapping and tracking techniques have advanced in complexity and applications: From tweezing single spheres or rods to the trapping of several particles in multiple traps, and, in recent years, to the trapping and 3D tracking of asymmetric, complex structures [14,23]. Here, we showed how 3D optical trapping and 3D interferometric tracking of a helical bacterium inside a line optical trap can be used for quantitative measurements on a broad temporal and spatial bandwidth.

#220691 - $15.00 USD Received 12 Aug 2014; revised 24 Sep 2014; accepted 25 Sep 2014; published 8 Oct 2014

The intent of this paper was to encourage other people from the optical trapping and tracking community to extend their setups for manipulation and force sensing of more complexly shaped objects. Therefore, we started with a section about the optical setup discussing the role of some special components. The most important part is a scan mirror (or alternatively, an acousto optic deflector), which generates a line shaped, time averaged optical potential. The focus distribution can be well adapted to the global shape of the trapped, lengthy object by controlling the position dependent transmission of the trapping laser beam. In this way, the object orients horizontally in the focal plane and can be well analyzed by imaging, e.g. based on scattered laser light.

The third section described the theoretical estimate of the local and global optical forces on a structure that can be modeled by a chain of pearls. Here we showed by numerical solution of the derived force expressions that, if the displacements are not too large, linear restoring forces act on each pearl of the chain. By assuming interconnecting springs between the pearls which are stiff relative to the trap stiffnesses, we could demonstrate that linear optical forces (harmonic potentials) act on the whole stiff object. We theoretically estimated the resulting trap stiffnesses of the linear forces using the equations introduced in the theory section and obtained a fairly good agreement to the experimentally obtained values. Linear restoring forces are the basis for most force sensing experiments using a straightforward trap calibration scheme.

Similarly, we could show that the interferometric signals also depend linearly on the positions of each slope of the helical bacterium. In other words, we derived the justification that the well-established BFP-interferometric tracking technique is also applicable for more complex structures, if a laser focus is scanned across the structure. This fast and precise tracking technique in the Fourier plane could not be used for static line-traps, e.g. holographical optical traps, if the same beam is used for trapping and tracking. Here, the light scattered at the whole object would result in a complicated interference pattern in the BFP and changes of the object in position, orientation or shape could only be recovered by using a camera in combination with inverse scattering approaches or model-based fitting.

Based on the expected linear dependency of both the optical force and the position signal on the displacement of a single slope of the bacterium, we developed a calibration scheme providing the force constants κ_i and the detector sensitivities g_i for all three directions $i = x,y,z$. Our approach is an extension of standard calibration methods used for spherical beads, such as the Langevin method to provide κ_i or bead-focus scans to determine g_i. Similarly we used position histograms and autocorrelation functions to characterize the dynamics of the helical bacterium in a 3D optical potential. In this way, we could determine the perpendicular and parallel friction factors of the helical structure which shows - and this is quite interesting - significantly reduced viscous drags relative to straight cylinders of a comparable size.

A time-multiplexed optical trap can be also adapted to other asymmetric objects. For lengthy, curved objects, the scanning laser focus can follow an arbitrarily curved line. For extended objects, the focus may scan even along an arbitrary height relief $\mathbf{r}_L(t) = (x,y,z(x,y))$. However, further investigations need to be done to uncover the relationship between the shape of an object and the linearity of the restoring forces.

The last section helps the reader to understand what boundary effects have to be taken into account to correct for calibration errors, when the diameter of the laser focus is broader than the sub-structures of the trapped object. For a freely diffusing bacterium we could achieve fast 2D scan experiments to verify the estimated correction factors. We hope that the ideas presented in this study will be inspiring to other optical trappers and trackers.

Acknowledgments

We thank Felix Jünger, Benjamin Tränkle and Lars Friedrich for helpful discussions. This study was supported by the Excellence Initiative of the German Federal and State Governments (EXC 294) and by the Deutsche Forschungsgemeinschaft (DFG), grant numbers RO 3615/1 and RO 3615/2.